Solidification of Sn-Pb alloys: Experiments on the influence of the initial concentration

L. Hachani, K. Zaidat, B. Saadi, X.D. Wang, Y. Fautrelle

Solidification of Sn−Pb alloys: Experiments on the influence of the initial concentration

L. Hachani [a], K. Zaidat [b, *], B. Saadi [b], X.D. Wang [c], Y. Fautrelle [b]

[a] *Mechanics Laboratory, University Amar Telidji of Laghouat, Algeria*
[b] *University of Grenoble, SIMAP-EPM, BP 75, 38402 Saint Martin d'Hères Cedex, France*
[c] *University of Chinese Academy of Sciences, Beijing, China*

A comparative study among solidification experiments for three selected alloys (Sn−3 wt.%Pb, Sn −6.5 wt.%Pb and Sn−10 wt.%Pb) was conducted on a benchmark experiment model under the same experimental conditions. The goal of this paper is to analyze the effect of variation in concentration on the solidification process with respect to different aspects: thermal, dynamic, structure, and morphology of segregation. Experimental results consist of instantaneous temperature maps provided by a lattice of 50 thermocouples welded on the large crucible side and post-mortem characterizations of the samples, such as X-ray imaging, solute local composition and metallography. Measurement of the instantaneous temperature field and numerical computation of liquid−solid interface evolution allows us to evaluate the effect of variation in concentration on thermosolutal convection behavior. Experimental results show that an increase in concentration greatly enhances the mechanism of the columnar-to-equiaxed tran-sition (CET) and leads to refinement of the equiaxed structure. However, a significant effect of solutal element (lead) stratification is observed, which can slow down thermosolutal convection, in particular for large concentrations. Especially, without any stirring lead segregation which likely occurs during the melting phase may suppress natural convection. Furthermore, lead stratification is significantly reduced when electromagnetic stirring is opposed to natural convection before the solidification phase begins.

1. Introduction

The behavior of the solidification process of metallic binary alloys is different from that of pure metal. First, solidification takes place over a temperature range and not at a fixed point. Second, solid and liquid zones are no longer separated by a distinct front, but by a complex region made up of dendrites and liquid, known as the mushy zone. Third, one component is preferentially rejected into the adjacent liquid zone to form a solute-rich layer at the interface front. A large number of experimental and numerical works have described the effects of such factors, such as control of cooling temperature (directional solidification) and initial concentration [1−3]: the main experimental parameters of controlled solidification are cooling rate (CR), temperature gradient (ΔT) and nominal concentration (C_0). A real solidification problem including heat and mass transfer and phase changes at different stages was described by a variety of authors such as Kurz and Fisher [4]. L.S. Chao et al. [5] studied experimentally the effects of different initial concentrations of Sn−Pb alloys on the final microstructure of the ingot. They observed a non-lamellar eutectic structure when initial concentration was closest to eutectic composition. Moreover, a transition mechanism between the columnar and equiaxed structure was also observed, the presence of which increases with initial concentration. Jin et al. [6] investigated in detail the effect of nominal concentration (C_0) on the size of the mushy zone, and revealed the extent of its influence, especially on solid fraction distribution. Nucleation of solidified grains, followed by growth occur when melt temperature drops below the nucleation temperature T_N which is below the liquidus temperature T_L. For further details the reader is referred to Kurz and Fischer [4]. When undercooling ($T_L - T_N$) exceeds the critical value required for formation of nuclei, the nucleation rate rises. In the case of equiaxed growth, the nucleation stage will continue until recalescence occurs. At the growth stage, grain radius increases due to adherence of liquid atoms to the solid/liquid interface until impingement takes place. In the impingement stage, the liquid between grains

* Corresponding author.
E-mail address: kader.zaidat@simap.grenoble-inp.fr (K. Zaidat).

solidifies, but the grain radii do not change. It is at this level that the final grain morphology is determined.

This present paper is based essentially on a comparative experimental study performed on a benchmark solidification experiment between three different Sn–Pb alloys (3%, 6.5% and 10%). These alloys are characterized by their thermo-physical properties available, as well as low liquidus temperature: 228.14 °C, 223.64 °C and 219.16 °C respectively. The purpose of this paper is primarily to investigate a controlled solidification experiment and to evaluate the effect of nominal concentration (C_0) on the fluid flow induced by thermosolutal convection and its consequence on macrostructures, solutal distribution and segregation morphology.

2. Experimental procedure

A benchmark solidification model is established and validated to study the effect of different concentrations on the solidification process. The experiment device consists in four major parts:

1 Fifty thermocouples were fixed on one of the largest surfaces of the crucible by laser-welding; on the opposite surface, the other sixteen thermocouples are arranged in the relative positions in order to calibrate temperature measurement. The interval distance in either the horizontal or vertical direction is 1.0 cm (see Fig. 1). Temperature fields and the evolutions are recorded during the melting/solidifying process by this thermocouple array. Note that all the thermocouples are in flush with the inner surfaces of the crucible to avoid any friction with the molten in the liquid state. The relative accuracy of the temperature measurement is ±0.1 K and, the response time of the thermocouples is 0.7 s, the recording time step was 1 s.

2 The newly designed heat exchangers yield novelty features: they have the same cross-sectional shape (1 cm × 6 cm) of the sample in the y-direction to ensure the heat flux release through them being more homogenous; the compact three part structure, cooper–stainless steel–cooper, is designed in order to shorten the heat transfer time; and to overcome chemical corrosion between tin and copper, two metal-layers Cr, Ni are deposited on the narrow vertical surfaces of the heat exchangers. The arrangement with nine thermocouples in each heat exchanger (Fig. 1), with a vertical distance of 2 cm and a horizontal distance of 1.5 cm, allows us to measure the heat flux.

3 An enclosure Kirchhoff box assures thermal insulation of the largest surface of the crucible via the heat radiation compensative method. This procedure is realized by a PID regulating system, the details can be found in Refs. [8,9].

4 The entire set-up is installed inside a vacuum chamber in order to limit heat transfer by air convection and protect the sample from oxidation; the degree of vacuum is of the order of 0.01 atm.

All samples consist of a 6 × 10 × 1 cm^3 rectangular ingot solidified by means of lateral cooling [7]. The entire experimental process of all solidification experiments consists of five steps illustrated in Fig. 2: melting, initial thermal stabilization to obtain a homogenous temperature field, application of experimental temperature difference ($\Delta T = 40$ K) between the two heat exchangers, second stabilization of temperature field to obtain a stationary fluid flow, followed by cooling of the sample at a fixed rate (CR = 0.03 K/s). During initial thermal stabilization, electromagnetic stirring can be used to homogenize the liquid sample. Stirring was mandatory to avoid probable lead stratification during the melting step. It was observed that, after melting and application of the temperature differences between the two lateral walls (i.e., step 4 in Fig. 2), without any stirring, temperature field distribution consisted of vertical isotherms as in a solid (see the temperature map presented in Fig. 3). This seemed to indicate that natural convection was practically suppressed by the existence of density stratification due to lead segregation during the melting step. This effect was more pronounced with a higher lead composition; e.g., 6.5% or 10%, as expected.

3. Results and discussion

3.1. Effect of concentration on thermosolutal convection

The temperature contours and gradients for an experimental study of the three compositions selected at different times during cooling are shown in Fig. 4 in the next section. The corresponding numerical values of the instantaneous temperature field are given in Appendix B. The experimental conditions are: $\Delta T = 40$ K, CR = 0.03 K/s. Fig. 4 illustrates the behavior of natural convection during the solidification process. Isotherm deflection provides some indication of the flow pattern generated by natural convection. As shown in Fig. 4(a), the flow pattern consists of clockwise recirculation. The temperature gradient (represented by arrows) on the crucible surface was calculated at each thermocouple position from the temperature difference between two adjacent points by means of a numerically centered difference scheme. The figure shows clearly the necessity of the electromagnetic stirring during the first phase of thermal stabilization (7000 s–11,000 s), before

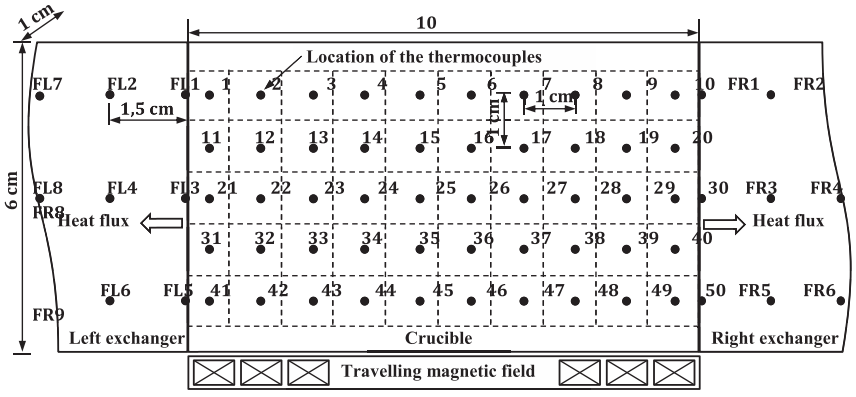

Fig. 1. Sketch of the solidification benchmark experiment: the location of the lateral thermocouples, the heat exchangers, and the traveling magnetic field.

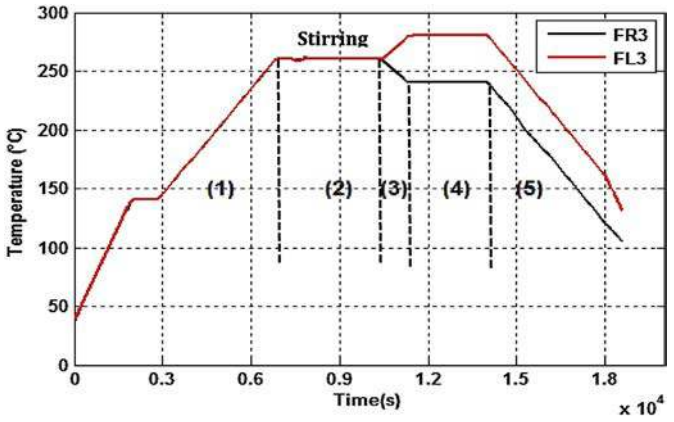

Fig. 2. Time evolution of measured temperature during solidification of thermocouples FR3 and FL3 located on the side of the heat exchangers as shown in Fig. 1. The process consists of five stages: (1) melting, (2) holding temperature to obtain a homogenous temperature field and electromagnetic stirring to homogenize the solute, (3) application of the average thermal gradient, (4) second stage of temperature field stabilization and (5) solidification.

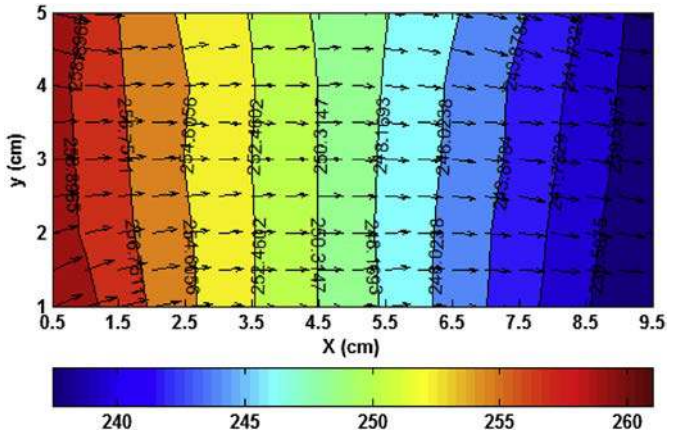

Fig. 3. Temperature field maps at time 14,000 s selected at second stage of thermal stabilization. Solidification experiment of Sn−10 wt.%Pb alloy released without any electromagnetic stirring. Temperature gradient ΔT = 40 K and cooling rate CR = 0.03 K/s. The liquidus temperature is T_l = 219.6 °C and solidus temperature T_s = 183 °C. The arrows correspond to the $(-\nabla T)$ vectors that are proportional to the local heat flux density.

the application of the experimental temperature difference (ΔT). Indeed, in the case of the Sn−10 wt.%PB alloy, convection is well established compared to the case of solidification of the same alloy without electromagnetic stirring shown in Fig. 3 at the same instant selected (t = 14,000 s) which represents the start of cooling. Fig. 4(a) shows that the convection loop presented by the deformation of the isothermal lines is well established in the case of Sn−3 wt.%Pb compared to the other alloys (Sn−6.5 wt.%Pb and Sn−10 wt.%Pb). The temperature difference between the maximum and minimum temperatures (T_{min} − T_{max}) for Sn−3 wt.%Pb is greater than 20 °C, but does not exceed 19 °C and 17 °C for Sn−6.5 wt.%Pb and Sn−10 wt.%Pb alloys, respectively. This result can be attributed to convection, which promotes heat transfer between the ingot and the two exchangers. In actual fact, the cooling phase occurs without electromagnetic stirring, since the three alloys underwent the same electromagnetic stirring for 1 h and 20 min during the initial thermal stabilization phase before application of the experimental mean temperature difference (ΔT = 40 K). The buoyancy-driven flow arises from density variations in the liquid due to the gradients in temperature and liquid composition, i.e. thermo-solutal convection. In the mushy zone, the relative strength of the thermal and solutal contributions can be found by calculating the buoyancy number N_B at a representative temperature of 200 °C. With the assumption of local thermodynamic equilibrium (lever rule), the temperature and liquid concentration are linked through the liquidus slope of the phase diagram, m (see Appendix A.1).

$$N_B = \frac{\textit{solutal buoyancy force}}{\textit{thermal buoyancy force}} = \frac{\partial\rho_l/\partial C_l}{\partial\rho_l/\partial T}\frac{\Delta C_l}{\Delta T} = \frac{\partial\rho_l/\partial C_l}{\partial\rho_l/\partial T}\frac{1}{m} = \frac{\beta_c \Delta C}{\beta_T \Delta T}$$
$$N_B|_{T=200^\circ C} = 8.31|_{3\%Pb} = 19.35|_{6.5\%Pb} = 27.8|_{10\%Pb} \quad (1)$$

where ΔC and ΔT, respectively, denote typical composition and temperature variations, and β_C and β_T the solutal and thermal expansion coefficients. The thermophysical properties of the Sn−Pb alloys are given in the equations below. The liquid density is from Ref. [19] and given in Eq. (2). The liquid viscosity is from Ref. [20] and shown in Eq. (3). The thermal conductivity of the liquid and solid phases, are from Ref. [21] and have been presented with the polynomial expressions given in Eqs (4) and (5). The diffusion coefficient in the liquid is from Ref. [22] and is shown in Eq. (6). For large buoyancy number values, solutal buoyancy forces are stronger than thermal forces. This proves that thermal and solutal buoyancy forces do not always work in the same direction. Consequently, solute sedimentation also plays a major role in solidification [9–11]. In these works [10], lead segregation occurs during the melting phase despite the use of electromagnetic stirring during the initial thermal stabilization step: stratification from top to bottom of the solute was significant, especially for concentrations exceeding 6.5%. For instance, this phenomenon was observed during melting of an alloy raw sample with a lead concentration of 10%wt. Consequently, prior to solidification, the buoyancy number was around 28, and natural convection was almost completely suppressed despite the applied thermal gradient (see Fig. 3).

$$\rho_l(C_l[\text{at\%}], T[\text{K}]) = 7359.5 + 47.6554C_l - 0.10063C_l^2 - \left(0.74284 + 5.8927\times10^{-3}C_l\right)T\left[\text{kg}/\text{m}^3\right] \quad (2)$$

$$\mu_l(C_l[\text{wt.\%}], T[\text{K}]) = A(C_l)\rho_{ref}^{1/3}\exp\left(\frac{b(C_l)\rho_{ref}}{T}\right)[\text{Pa s}],$$
$$\begin{cases} A(C_l[\text{wt.\%}]) = 2750\times10^{-4} - 2934\times10^{-6}C_l + 1.212\times10^{-7}C_l^2 - 1.56\times10^{-9}C_l^3 \\ b(C_l[\text{wt.\%}]) = 8849 + 0.9411C_l - 4.193\times10^{-2}C_l^2 - 5.3\times10^{-4}C_l^3 \end{cases} \quad (3)$$

$$\lambda_l(C_l[\text{wt.\%}]) = 25 + 0.02T - 0.35C_l + 0.002C_l^2[\text{W/(m K)}] \quad (4)$$

$$\lambda_s(C_l[\text{wt.\%}]) = 64.74 - 0.016T - 0.543C_s + 0.0023C_s^2[\text{W/(m K)}] \quad (5)$$

$$D_l(T[\text{K}]) = 1.4 \times 10^{-7} \exp\left(-\frac{2.29 \times 10^4}{RT}\right)\left[\text{m}^2/\text{s}\right] \quad (6)$$

The second selected time (t = 16,400 s), shown in Fig. 4(b), is the last solidification stage for the alloy Sn 3 wt.%Pb, such that the temperature map shows a temperature average of 188.8 °C close to the eutectic temperature (T_E = 183 °C). The local temperature gradient vectors are almost identical, thus confirming the dominance of conduction as the heat transfer mode. However, the two remaining alloys exhibit an average temperature in the vicinity of 197 °C, thereby proving the existence of a convection loop still completely active to the left of these ingots, corresponding to the last liquid. Temperature maps thus show the emergence of a second solidification front, particularly in the case of 6.5%wt. This second front is responsible for the creation of a second convection loop to the far left of the ingots, accounting for the different shrinkage types corresponding to the last liquid solidified, which will be presented in the next section.

3.2. Effect of concentration on the velocity field

To study the effect of concentration on fluid flow, temperature data are analyzed to obtain an estimate of the magnitude of the velocity field during solidification in the liquid zone. This method

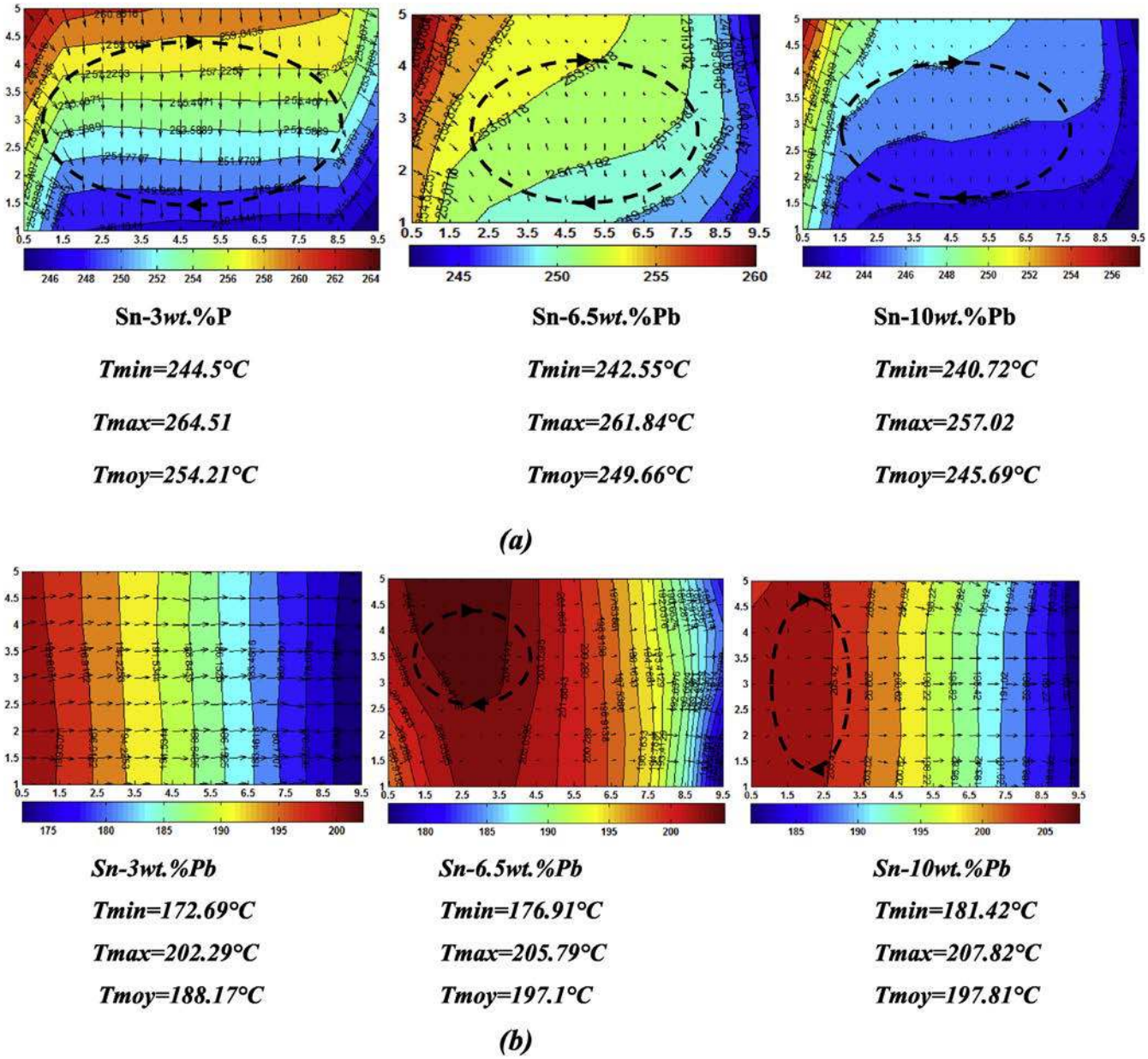

Fig. 4. Time evolution of temperature fields coupled to the temperature gradient vectors (black arrows) at different times chosen (t = 14,000 s (a) and t = 16,400 s (b)) for the three alloys Sn–3 wt.%Pb, Sn–6.5 wt.%Pb and Sn–10 wt.%Pb. Experimental conditions: experimental average temperature difference ΔT = 40 K, cooling rate CR = 0.03 K/s. Electromagnetic stirring used only during the first thermal stabilization phase.

consists in calculating velocity field projection on the temperature gradient vector at each node corresponding to a thermocouple location. The principle of the method is described below.

The integration of the heat equation on the sample thickness in the liquid zone is:

$$\int_0^e \frac{\partial T}{\partial t} dz + \int_0^e \vec{u} \cdot \vec{\nabla} T dz = \alpha \int_0^e \nabla^2 T dz, \tag{7}$$

where $\vec{u}$, α and e respectively denotes the instantaneous velocity field, the liquid thermal diffusivity and the sample thickness. If we assume that the temperature field is uniform in the transverse direction thus two-dimensional, then the integral (7) reduces to:

$$\frac{\partial T}{\partial t} + \vec{U} \cdot \vec{\nabla} T = \alpha \nabla^2 T \quad \text{with} \quad \vec{U} = \frac{1}{e} \int_0^e \vec{u} dz \tag{8}$$

The vector $\vec{U}$represents the average of the instantaneous velocity across the sample thickness. The algebraic velocity estimate U is defined as $U = \vec{U} \cdot \vec{\nabla} T / (|\nabla T|)$where $|\nabla T|$is the norm of the temperature gradient. Fig. 5 shows velocity projection time evolution on the thermal gradient vector for various internal nodes selected. The value of U is obtained by discretizing the heat equation at liquid state (without latent heat release) and introducing the measured temperature data. A finite difference method is used for space discretization, while a leap frog scheme is used for time. Details of the method are provided in Appendix C and the results are shown in Figs. 5 and 6 for the three alloys mentioned above, and experimental condition are $\Delta T = 40$ K and CR = 0.03 K/s. Analysis of the velocity profiles (e.g., in Fig. 5) indicates that the velocity estimate is less than 0.5 cm/s for all cases. Furthermore, the method is no longer valid when equiaxed grains appear near the end of solidification. However, the present estimation is likely to be significantly lower than maximum convective velocity. According to the numerical calculations of this configuration made by R. Boussaa et al. [12], the velocity magnitude is around 1–2 cm/s for a thermosolutal convection. As the Peclet number is relatively high, typically 36 for a velocity magnitude of 1 cm/s, isotherms are significantly deflected by the flow, thus decreasing velocity projection. The typical order of magnitude for velocity projection is 2–5 mm/s.

Fig. 5 shows velocity projections as a function of time at different positions (nodes 14–18), where velocity vector ($\|\vec{U}\|$) and temperature gradient ($\vec{\nabla} T$) scalar products are not assumed to be too small. A variety of observations can be made concerning this analysis. First, the various solidification process steps are retrieved, namely global stabilization of velocity during the thermal convection regime before cooling. Second, velocity decays when the columnar front approaches the node. In point of fact, if one node is considered (for example node 14 for the three cases in Fig. 5), during the solidification phase, velocity magnitude can be seen to increase significantly before dropping to nearly zero. This is attributed to convection just before the assumed passage of the columnar front. Numerical calculations have proved, T. Carozzani [13] that convective flow is quite peculiar at low Prandtl numbers, and consists of a recirculating jet. This pattern is qualitatively validated by the observations. We have determined the instant when velocity decreases to a value close to zero by fitting algorithms and extrapolating the velocity curve to zero using the calculated tangent at the inflection point (see Fig. 6, for example). This procedure was justified by the fact that the present method ceases to be valid when the node coincides with the columnar front, due to latent heat release that has not been taken into account. These instants (noted Tag14 for node 14 and so forth) are shown in Fig. 6. Note that the time sequence is consistent with node position and enables us to follow the columnar front. An estimation of columnar front velocity can be obtained from transit time, e.g. (Tag15_Tag14) of the front from node between two thermocouples, say 15 to 14. Moreover, temperature estimation can be obtained when the columnar front reaches a thermocouple. These results show that columnar front temperature is less than nominal liquidus temperature of the alloy by approximately 2–10 K. Thus, a significant effect of concentration on the velocity profile was observed, in particular during the corresponding phase thermal convection. Indeed for node 14, fluctuation of the velocity projected is lower (in absolute value) than 0.5 cm/s, however it does not exceed the values of 0.25 cm/s and 0.15 cm/s for 6.5 and 10% concentrations, respectively.

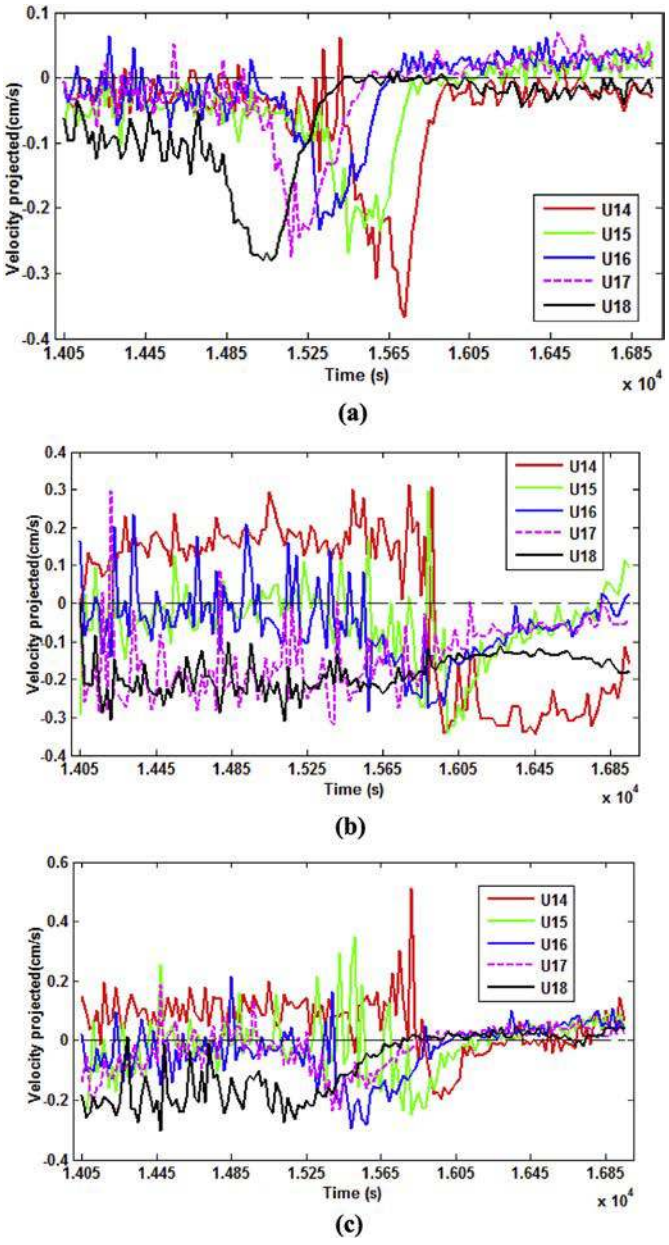

Fig. 5. Velocity estimate U versus time for various internal nodes (14, 15, 16, 17and 18) located in the upper part of the ingot. (a) Sn–3 wt.%Pb, (b) Sn–6.5 wt.%Pb and (c) Sn–10 wt.%Pb. Experimental condition $\Delta T = 40$ K, CR = 0.03 K/s.

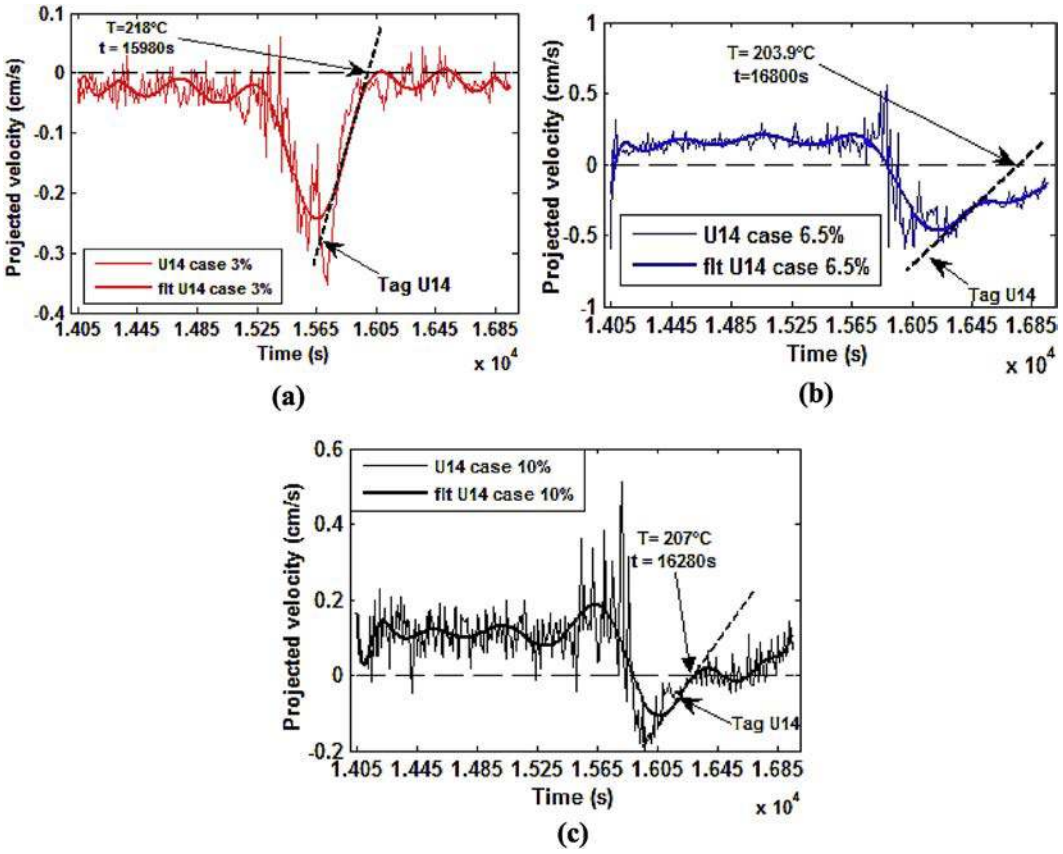

Fig. 6. Velocity curve for node 14: (a) Sn−3 wt.%Pb, (b) Sn−6.5 wt.%Pb and (c) Sn−10 wt.%Pb. Fig. 5 also shows the fitting curve for the three cases as well as the extrapolation to zero used to estimate the instant when the columnar front crosses the node position.

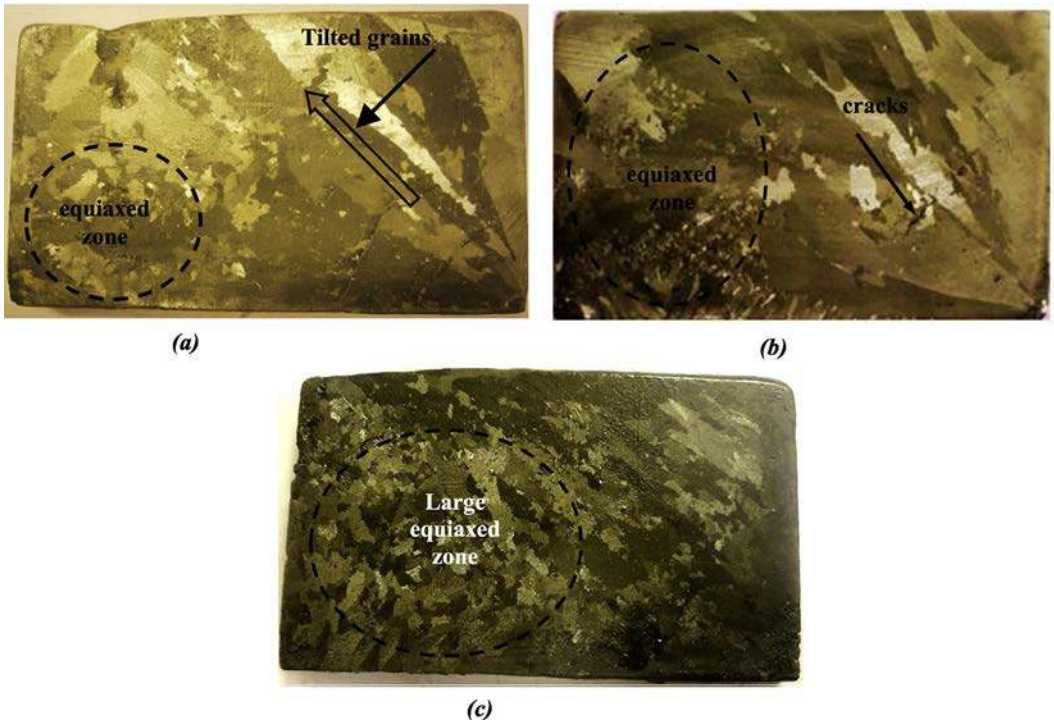

Fig. 7. Macrostructure on the lateral plane of ingots: (a) Sn−3 wt.%Pb, (b) Sn−6.5 wt.%Pb and (c) Sn−10 wt.%Pb. Experimental conditions: average temperature difference $\Delta T = 40$ K and a cooling rate CR = 0.03 K/s.

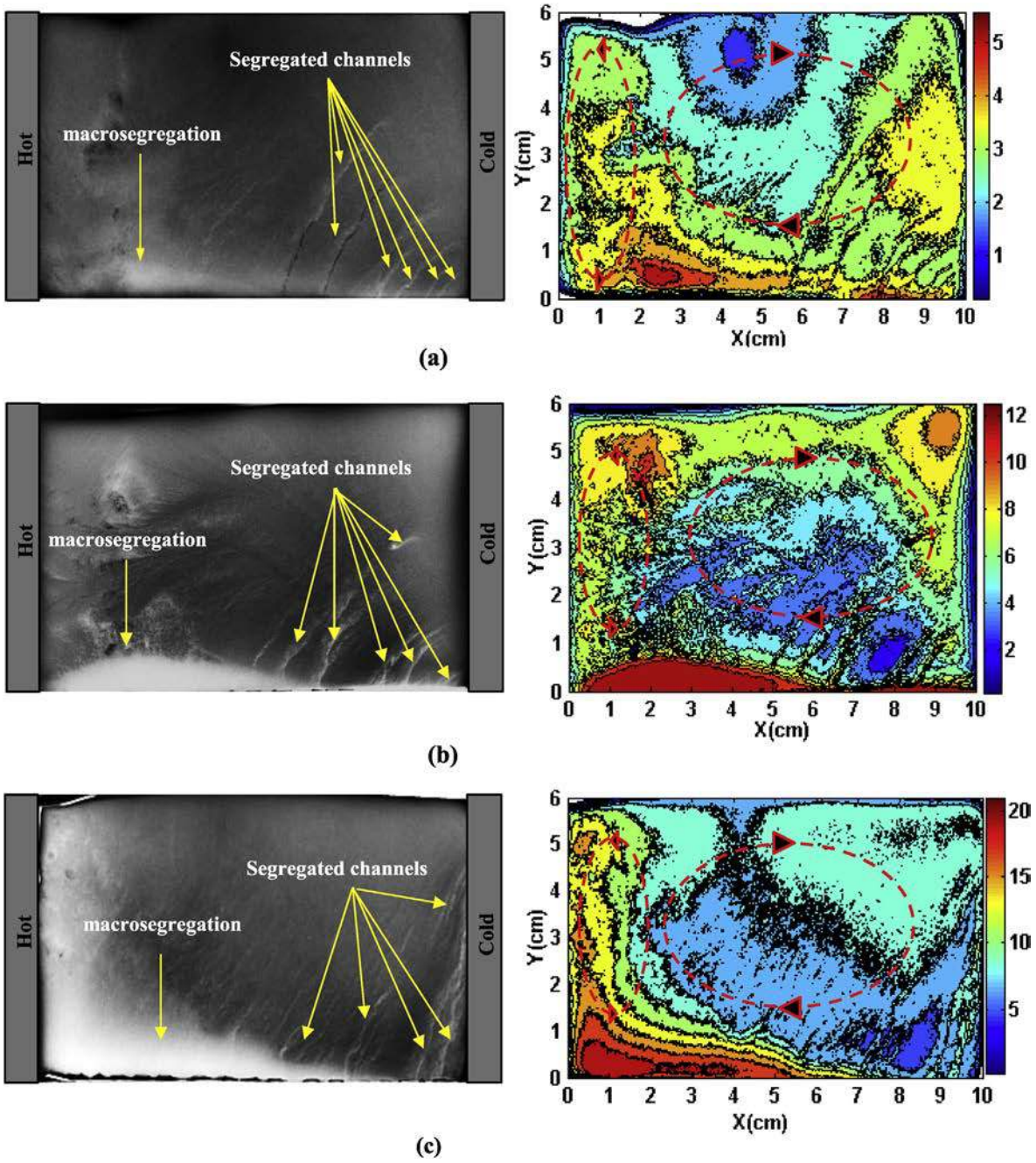

Fig. 8. X-rays of the solidified ingot showing the lead segregations (in white) for (a) Sn−3 wt.%Pb, (b) Sn−6.5 wt.%Pb and (c) Sn−10 wt.%Pb alloy. Freckles are visible in the right part of the samples. Experimental conditions are: $\Delta T = 40$ K, CR = 0.03 K/s.

3.3. *Effect of concentration on the macrostructure*

The corresponding macrostructures of this comparative study among the three alloys are illustrated in Fig. 7. Macrostructures are obtained after post mortem analysis, which consists of several passes of polishing and chemical attack with a mixture of 75% Vol HCL (37 mol%/v) and 25% Vol HNO_3 (69.5%). Fig. 6 shows that solidification starts with a large columnar zone followed by a columnar-to-equiaxed transition (CET) in all cases. Upstream tilting of the columns is a consequence of a downward flow along the columnar front. Presence of equiaxed grains is progressively more visible as concentration increases (see for example Fig. 7(b) and (c)). The equiaxed grains in the Sn−10 wt.%Pb are observed to have smaller sizes and to occupy a larger area compared to the previous cases with relatively lower concentrations, 3% and 6.5%. The emergence of an equiaxed zone is the result of several factors including two main causes, namely decay of the temperature gradient ahead of the columnar front and an increase of the front velocity. Indeed, Fig. 4(b) shows the significant decrease of the temperature gradient in the last liquid in the sample during almost the end of the process. Secondly, in the work of Hachani et al. [8], the analysis carried out by the method of the velocity projected indicates that the columnar front velocity globally increases as of solidification proceeds. Such both events are favorable as far as the appearance of the Columnar-to-Equiaxed Transition (CET) is concerned. In the present cases, both mechanisms occur in the

experiments near the end of solidification. This result can also be attributed to the effect of an increase in concentration, promoting fragmentation dendritic arms through dissolution, caused by variations in solutal gradient in the mushy zone as described by Liu [14]. This hypothesis was reinforced by the work of Gu and Beckermann [15], who studied fragmentation during formation of segregated channels as freckles during solidification, and attributed the formation of fragments to the dendrite solutal dissolution process.

3.4. Effect of concentration on the morphology of segregation

Post-mortem X-ray radiographs were performed on different solidified tin–lead alloys at the CEA Saclay (Paris). The X-ray principle is based on the difference in density between lead and tin, leading to differences in X-ray absorption that have enabled us to establish gray scale maps of lead concentration in the solid. These maps are averaged over sample thickness. The lighter areas correspond to the richest areas of lead, while the darker ones correspond to the poorest areas. Due to the relatively large thickness of the sample, it was necessary to use a high power setup (Philips MCN321, 300 kV). The experimental results of the concentration expressed in pixels are converted into mass concentration by a digital image processing with MATLAB software. The main goal is to observe the effect of concentration on all types of macro–meso segregation and, in particular, on the distributions of segregated channels that are very hard to track from the point of view of formation, morphology and distribution. A comparative study based on X-ray images and their digital processing for all three ingots (Sn–3 wt.%Pb, Sn–6.5 wt.%Pb and Sn–10 wt.%Pb) was conducted and is shown in Fig. 8. The effect of lead stratification is very significant in ingots with a relatively high concentration (6.5 and 10%) compared to Sn–3 wt.%Pb. The result is a wide stratification zone spread over the bottom of the ingot Sn–10 wt.%Pb with a concentration of up to 21% and 12% for Sn–6.5 wt.%Pb. This segregation zone appears only in the last liquid at the end of solidification of the Sn–3 wt.%Pb ingot with a chimney form where the level of concentration does not exceed 4.8%.

Furthermore, the experimental results illustrated in Fig. 8 confirm the existence of several segregated channels located to the right of all samples. Segregated channels are several centimeters long and a few millimeters thick. Fluid flow within the mushy zone is probably responsible for this segregation. Natural convection transports the heavier solute from the bulk to the bottom left-hand part of the ingot. As shown in Fig. 8, segregated channel behavior depends on initial concentration. A macrosegregation

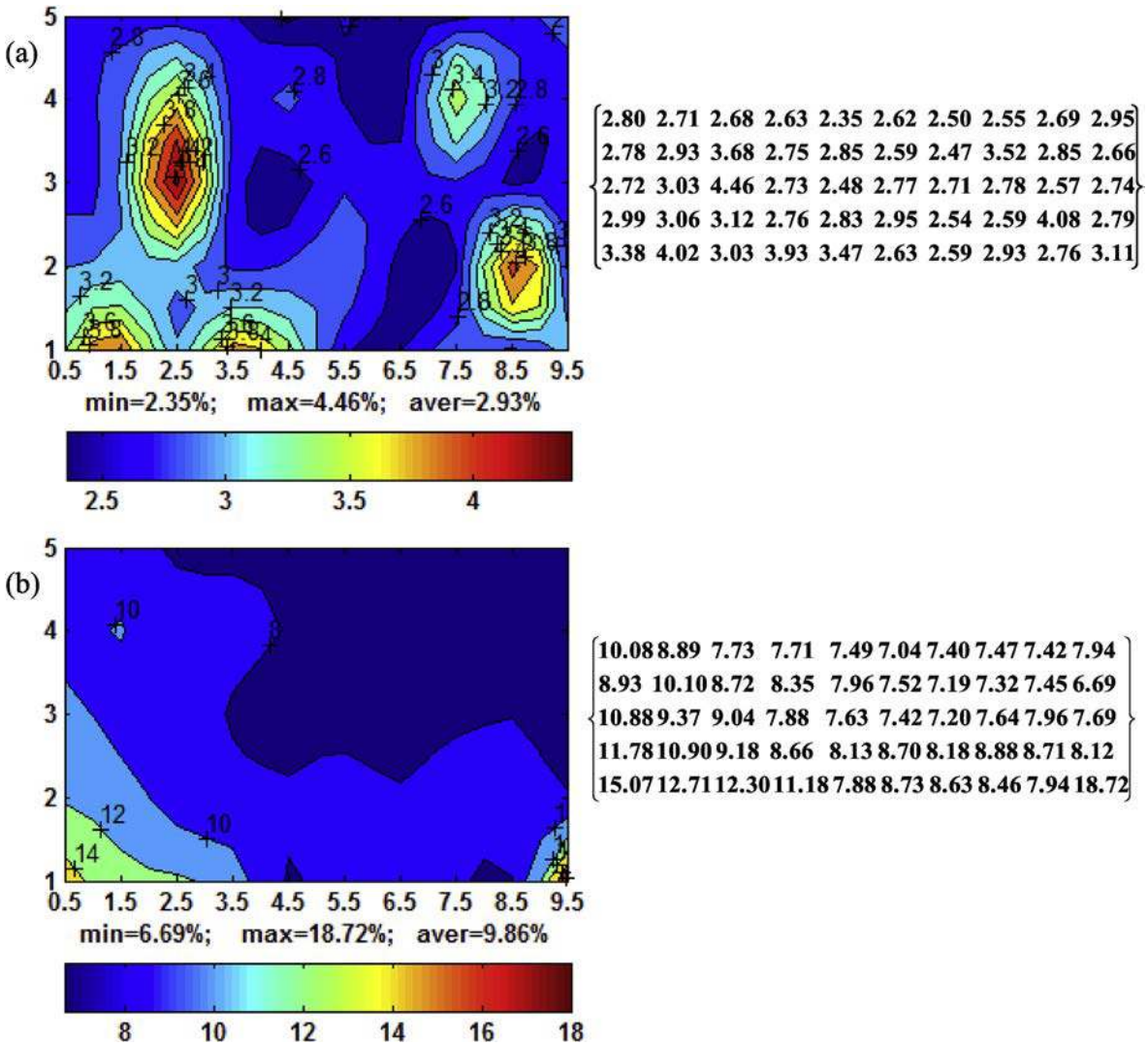

2.80	2.71	2.68	2.63	2.35	2.62	2.50	2.55	2.69	2.95
2.78	2.93	3.68	2.75	2.85	2.59	2.47	3.52	2.85	2.66
2.72	3.03	4.46	2.73	2.48	2.77	2.71	2.78	2.57	2.74
2.99	3.06	3.12	2.76	2.83	2.95	2.54	2.59	4.08	2.79
3.38	4.02	3.03	3.93	3.47	2.63	2.59	2.93	2.76	3.11

10.08	8.89	7.73	7.71	7.49	7.04	7.40	7.47	7.42	7.94
8.93	10.10	8.72	8.35	7.96	7.52	7.19	7.32	7.45	6.69
10.88	9.37	9.04	7.88	7.63	7.42	7.20	7.64	7.96	7.69
11.78	10.90	9.18	8.66	8.13	8.70	8.18	8.88	8.71	8.12
15.07	12.71	12.30	11.18	7.88	8.73	8.63	8.46	7.94	18.72

Fig. 9. Lead concentration maps (left) and corresponding numerical values (right) for (a) Sn–3 wt.%Pb and (b) Sn–10 wt.%Pb. Applied temperature difference $\Delta T = 40$ K and cooling rates CR = 0.03 K/s.

zone, with a chimney form corresponding to the last liquid solidified, was observed in almost all X-ray images. This paper suggests that this geometric shape is the result of two convection loops at the end of solidification. These results match the temperature maps shown in Fig. 4(b). However, we note that the number of segregated channels is higher: 10% compared to 3%. The X-ray radiography of the ingot Sn−6.5 wt.%Pb shows a particular shape and size of the segregated channels (see Fig. 8(b)). In actual fact, it is difficult to know whether this particular shape is due to stratification generated by heavy lead compared to solvent (tin), or to stacking of a set of segregated channels on ingot thickness.

3.5. *Effect of concentration on solutal distribution*

A chemical method coupled with the inductively coupled plasma (ICP) technique is used to quantitatively analyze lead concentration distribution. Fifty holes are made at the location of the thermocouples (Fig. 1.) on the three samples to extract roughly 200 mg for each analyzed sample. The relative error on the concentration measurement values is ±3%. The results illustrated in Fig. 9 show segregation distribution for two selected alloys (3 and 10%) for experimental condition ($\Delta T = 40$ K, CR = 0.03 K/s). We checked that the measured average concentration was close to the nominal values. The average values are provided in Fig. 9 together with the local composition values measured. Based on the results obtained by quantitative analysis of lead distribution in the two ingots analyzed, some findings and general conclusions on segregation morphology were determined. In all cases, solute rejection starts at the right side of the sample, meaning that, at the end of solidification, an enriched lead area appears on the bottom left-hand side. We verified that the average concentration of all measured ingots was close to the nominal concentration (2.93% for the Sn−3 wt.Pb alloy and 9.89% for the Sn−10 wt.%Pb alloy). However, the maps show a wide variety of lead distribution in each case. For example, the Sn−3 wt.%Pb alloy map indicates the existence of segregated channels on the right side (cold side) of the ingots with a level of concentration ranging between 4.2 and 4.4%. The same applies for the Sn−10 wt.%Pb alloy in the bottom right-hand corner with a concentration of more than 18%. The position and shape of the macrosegregation area corresponding to the last liquid have also changed. For example, for the right map (3%), the macrosegregation area is located at almost 2.5 cm with a chimney form, compared to the other map (10%),which is near the end on the left side of the ingot (hot side). This variation can be justified by the development of the second solidification front on the left side (hot side), which varies from one experiment to another. The latter

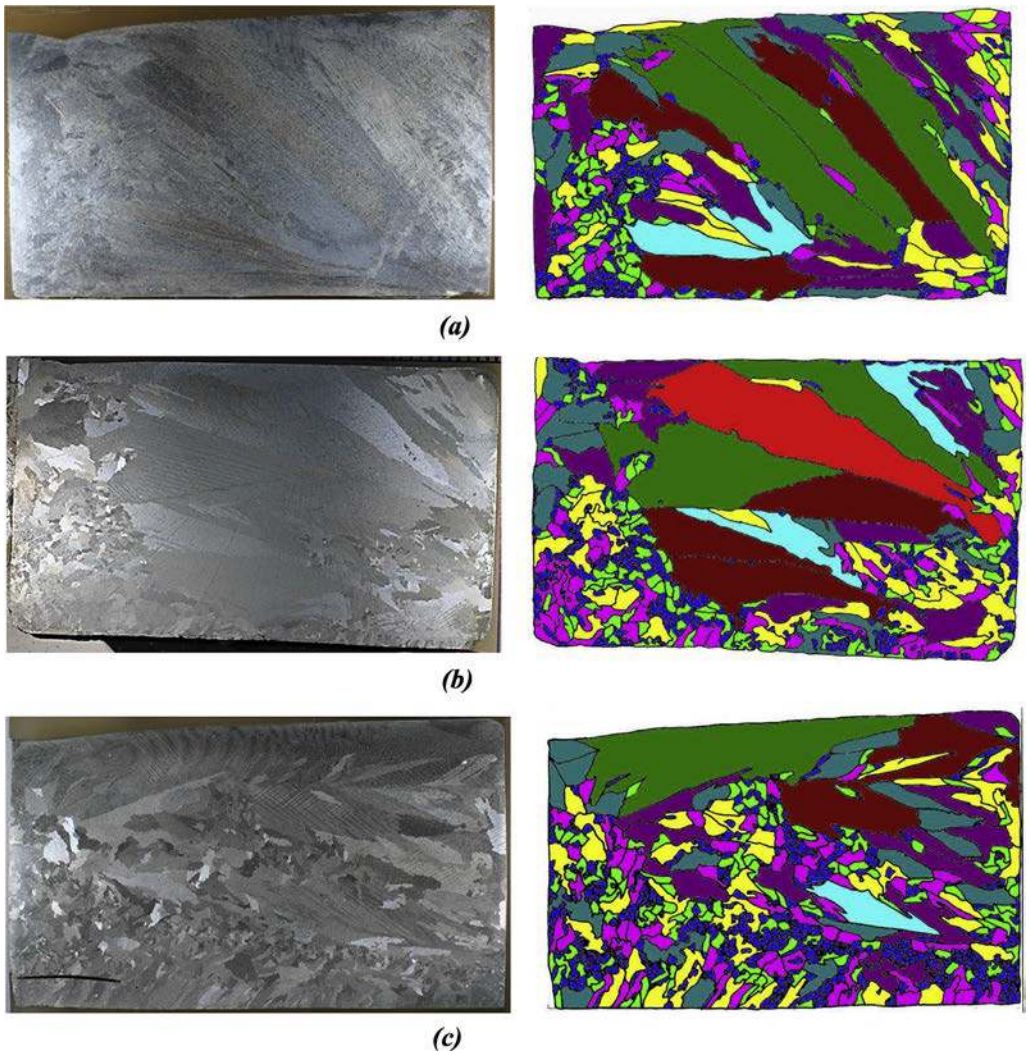

Fig. 10. Macrostructure left and its grain contour for (a) Sn−3 wt.%Pb, (b) Sn−6.5 wt.%Pb and (c) Sn−10 wt.%Pb alloy. Experimental conditions are: $\Delta T = 40$ K, CR = 0.03 K/s. Experiments conducted without electromagnetic stirring during the melting step.

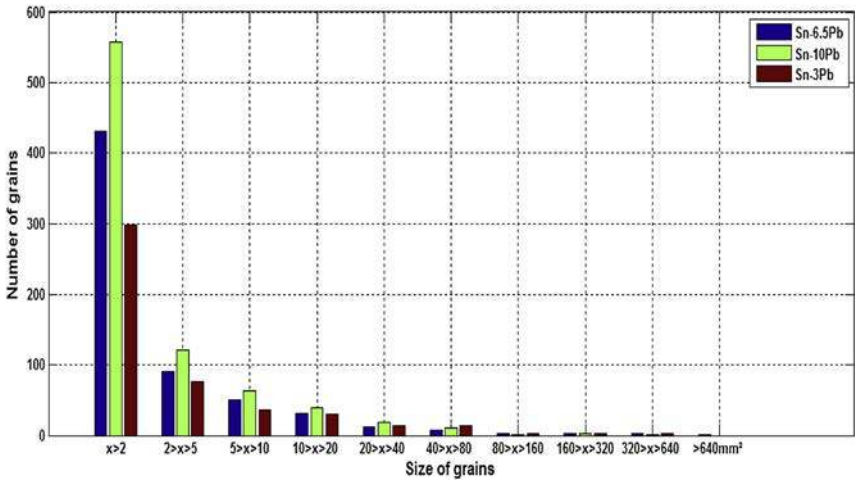

Fig. 11. Distribution of grain size for the three samples: Sn−3 wt.%Pb, Sn−6.5 wt.%Pb and Sn−10 wt.%Pb alloy. Experimental conditions are: $\Delta T = 40$ K, CR = 0.03 K/s.

observation is consistent with the isotherm distribution shown in Fig. 4(b).

3.6. Effect of concentration on the grain structure and eutectic fraction

Analyses other than X-rays were conducted to establish grain structure and verify the effect of increasing composition on the final crystal structure. Fig. 10 shows the grain iso-contours for the three alloys treated in this study. The analysis was conducted at the Critt METALL 2T Nancy research center. The sample was polished according to a specific procedure based on tin alloys (polishing with an ethylene-glycol mixture) and a chemical attack using a solution of 80% glycol, 10% nitric acid and 10% acetic acid. As the solute lead composition increases, the columnar dendrite growing angle decreases and the CET macrostructure increases, as observed in Fig. 7. However, macrostructure observations show a significant difference in size between the grains. A graphic representation of the number of grains based on their size is given in Fig. 11 for the three alloys. The geometric characteristics of the macrostructure are summarized in Appendix D. The results clearly show that the increase in solutal element (lead) greatly enhances the columnar-to-equiaxed transition (CET), thereby refining equiaxed grains. This is observed by the dominance of the number of grains less than 40 mm^2 in the case of the Sn−10 wt.Pb alloy compared to the other ingots. This paper proposes that the predominant mechanism responsible for blocking progress of the columnar front is solutal blocking, due to solute rejection by equiaxed grains during solidification as proposed by Martorano et al. [16]. As the rejected solute enriches the inter-dendritic liquid, the concentration gradient, which is the driving growth force, will gradually decrease. Grains will grow and then slowly stop growing without coming into direct contact with one another [16–18].

Fig. 12 illustrates distribution of the eutectic fraction and microstructure for all three different lead concentrations (3%, 6.5%, and 10%). Experimental conditions are: average experimental temperature difference $\Delta T = 40$ K, cooling rate CR = 0.03 K/s. We also characterized the Secondary Dendrite Arm Spacing (SDAS) of these alloys. The primary solid solution "not attacked by the chemical solution" was thresholded, and our measurements taken using an optical microscope. These measurements taken by thresholding dendrites are illustrated in the example shown in the micrograph presented in Fig. 11. Secondary dendritic arm spacing (λ_2) was measured in three zones for each sample (left, middle and right). We checked that the microstructure did not change with time for a typical duration of several months presented in Fig. 12(a). The results are given in Appendix E, where each value represents an average of 25 measurements. The average values measured vary between 93, 90 and 69 for the cases of Sn−3 wt.%Pb, Sn−6.5 wt.%Pb and Sn−10 wt.%Pb, respectively. SDAS appears to decrease as concentration increases.

4. Conclusion

A comparative study treating the effect of different concentrations on the tin−lead alloy solidification process at three concentrations (3%, 6.5% and 10%) was experimentally investigated in this work. Instantaneous temperature distributions were recorded and analyzed, and detailed post-mortem characterizations were compiled. Several aspects are examined especially thermal, dynamic, structure (CET) and final segregation morphology. Experimental benchmark set up provide reference data needed for scientific community, especially those interested to the modeling of metallic alloys solidification process.

The analysis of the temperature field allowed quantitative data to be obtained on melt convection as well as the solidification front dynamics. Based on the post-mortem analysis, various types of macrostructure were obtained, i.e., columnar and equiaxed. The columnar-to-equiaxed transition was observed for all compositions. The results clearly showed the existence of two types of segregation: the first takes the form of segregated channels located in the first layers of solids formed, while the second, known as a normal segregation zone, corresponds to the last liquid at the end of solidification, which has assumed, in most cases, a chimney form due to macrosegregation. A significant effect of concentration on the number of segregated channels and the size of the second area macrosegregation was observed. The experimental results allowed us to conclude that, for solidification, experiments with a high lead concentration (10% and more) have a dual effect: stratification lead at the base of the ingot and formation of a wide area of refined equiaxed grains. The traveling magnetic field (TMF) here is only used to enhance the thermo-solutal convection for the high value of concentration only in a short period before the solidification step. Without any stirring lead segregation which likely occurs during the melting phase

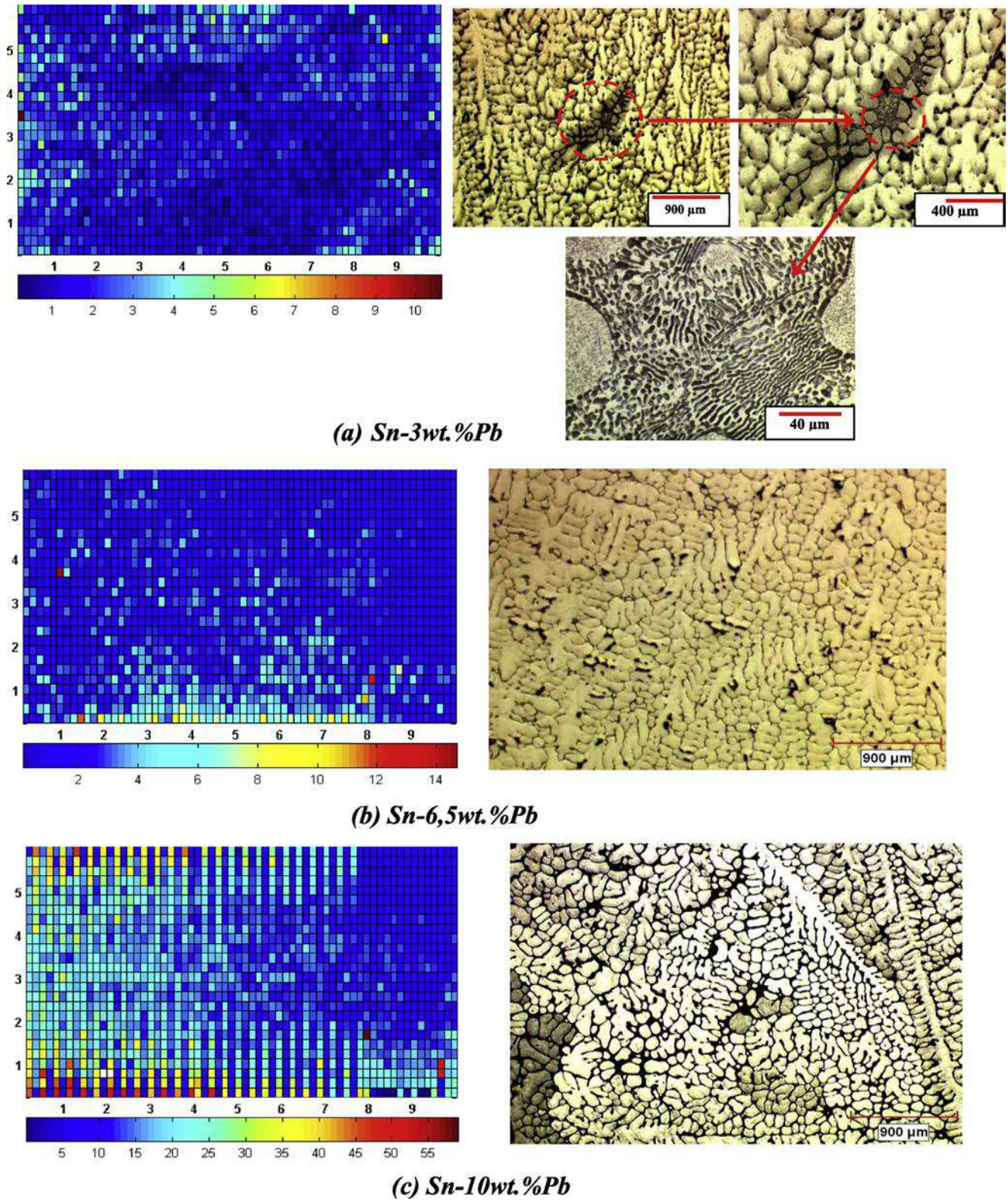

Fig. 12. Left eutectic fraction and right microstructure, for the samples (a) Sn−3 wt.%Pb, (b) Sn−6.5 wt.%Pb and (c) Sn−10 wt.%Pb. Experimental conditions: $\Delta T = 40$ K, CR = 0.03 K/s.

may suppress natural convection. Finally, the experimental and analytical study confirmed the need for application of controlled electromagnetic stirring to control the heterogeneity defect in concentration (segregation), or even to eliminate such defects completely.

Acknowledgments

The authors extend their thanks to the European Space Agency via the CETSOL project (ESA-MAP AO-99-117) as well as the SMACS ANR project for their financial support. The authors are indebted to

B. Rattoni (CEA-Saclay, France), who carried out the X-ray characterizations.

Appendix A

Appendix A.1. Phase diagram of Sn–Pb alloy

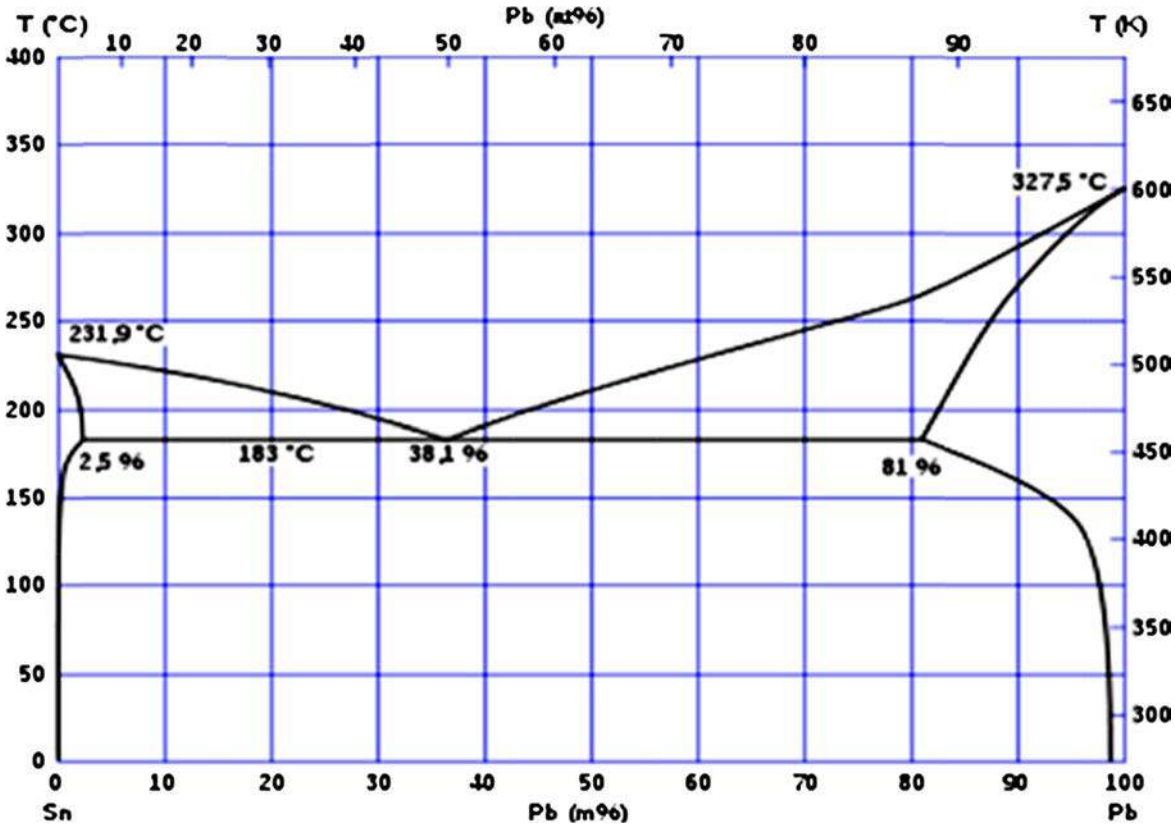

Appendix A.2. Thermophysical properties

	Sn	Pb	Sn–10%Pb	Sn–6.5%Pb	Sn–3%Pb	Unit
Liquidus temperature	231.97	327.5	219.16	223.46	228.14	°C
Solidus temperature	231.97	327.5	183.42	183.42	183.42	°C
Partition coefficient	–	–	0.0656	0.0656	0.0656	–
Liquidus slope	–	–	−1.2826	−1.2826	−1.2856	K/pbs
Eutectic composition	–	–	38.1	38.1	38.1	Pds
Eutectic temperature	–	–	183.42	183.42	183.42	°C
Liquid density	7000	10,678	7480	7380	7110	kg/m^3
Solid density	6670	11,700	7840	7720	6821	kg/m^3
Specific heat of liquid	250 at (232 °C) 242 at (300 °C) 241 at (400 °C)	152 at (327 °C) 144 at (400 °C) 137 at (500 °C)	243	259	265	$J\ kg^{-1}\ K^{-1}$
Specific heat of solid	–	–	209	221	226	$J\ kg^{-1}\ K^{-1}$
Latent heat	60,697		56,140	57,120	57,512	J/kg
Thermal conductivity in liquid	30	15.4 (327 °C)	27	26	25	$W\ m^{-1}\ K^{-1}$
Thermal conductivity in solid	60	29.7 (300 °C)	63	64	64	$W\ m^{-1}\ K^{-1}$
Thermal expansion coefficient	2.35E-05		6.60E-05		9.5E-5	K^{-1}
Solutal expansion coefficient			−4.20E-04		−5.3E-3	(pds^{-1})
kinematic viscosity	2.73E-7	0.001	2.67E-07		0.002	m^2/s
Dynamic viscosity	0.00191		0.001			$kg\ m^{-1}\ s^{-1}$

Appendix B. Instantaneous temperature maps recorded for three selected times corresponding to the experiments Sn−3 wt.%Pb, Sn−10 wt.%Pb and Sn−6.5 wt.%Pb. Experimental conditions: ΔT = 40 K, CR = 0.03 K/s.

	Experiment	Temperature maps (°C)									
14,000 s	Sn−3 wt.%Pb	264.49	261.69	261.09	261.08	260.39	260.49	260.09	259.69	259.19	254.19
		261.99	257.99	257.79	257.78	257.69	257.59	257.49	257.48	257.59	252.59
		258.79	254.39	253.99	254.09	254.29	254.19	254.39	254.19	254.39	250.09
		256.39	250.89	250.59	250.69	250.89	250.99	250.89	250.59	250.79	247.29
		254.09	248.29	247.99	247.79	247.49	247.59	247.09	247.08	247.18	244.49
	Sn−10 wt.%Pb	257.02	250.42	248.22	247.52	247.02	247.12	246.62	246.12	245.22	241.32
		253.92	248.52	247.22	246.52	246.72	246.52	246.22	245.92	245.52	242.72
		251.62	246.72	245.82	245.52	245.62	245.52	245.22	245.23	244.92	242.52
		250.32	245.42	244.62	244.42	244.43	244.22	244.02	244.03	243.82	241.92
		249.02	244.12	243.52	243.22	243.12	243.13	242.82	242.72	242.52	240.72
	Sn−6.5 wt.%Pb	255.60	251.90	251.01	250.59	250.16	249.65	249.25	248.69	246.77	243.26
		256.13	253.10	252.08	251.71	251.31	251.11	250.82	250.20	248.86	246.35
		257.29	254.51	253.25	252.84	252.40	252.32	252.10	251.35	249.99	245.94
		259.97	256.02	254.47	253.57	253.26	252.97	252.68	251.84	249.60	243.92
		261.84	257.12	255.43	254.50	253.72	253.50	252.87	251.82	249.11	242.55
14,800 s	Sn−3 wt.%Pb	245.79	243.49	243.09	242.89	242.49	242.48	242.39	241.79	240.99	233.99
		243.59	240.49	240.19	240.29	240.28	240.19	239.99	240.09	239.29	230.49
		240.89	237.39	237.09	237.29	237.49	237.48	237.29	237.28	236.19	227.39
		239.19	234.39	234.19	234.39	234.79	234.69	234.68	234.29	232.89	225.09
		236.89	232.09	232.08	231.99	231.97	231.98	231.79	231.59	229.59	223.99
	Sn−10 wt.%Pb	237.12	231.92	230.22	229.42	229.43	229.02	228.72	228.12	226.92	221.92
		234.12	229.82	228.62	228.22	228.23	228.12	227.72	227.62	226.92	223.42
		231.82	227.92	227.42	227.12	227.02	226.92	226.62	226.52	226.12	223.12
		230.62	226.52	225.92	225.62	225.82	225.52	225.32	225.02	224.92	222.32
		229.32	225.12	224.72	224.32	224.33	224.22	223.62	223.42	223.12	220.92
	Sn−6.5 wt.%Pb	237.03	233.66	232.77	232.35	231.87	231.42	231.08	230.25	228.30	224.41
		237.51	234.80	233.93	233.36	233.14	232.94	232.72	231.93	230.53	227.65
		238.58	236.23	235.15	234.62	234.39	234.22	233.86	233.15	231.68	227.29
		241.04	237.72	236.55	235.55	235.33	235.07	234.65	233.76	231.47	225.13
		242.82	238.97	237.53	236.70	236.10	235.68	234.98	233.75	230.88	223.77
16,400 s	Sn−3 wt.%Pb	201.29	198.19	195.89	192.89	190.69	186.79	183.69	179.89	176.69	173.79
		201.39	198.69	195.79	193.19	190.29	186.89	183.59	180.19	176.59	172.99
		201.99	199.09	196.29	193.19	190.49	187.19	183.59	180.19	176.29	172.79
		202.29	199.49	196.49	193.39	190.89	187.29	184.09	179.79	176.49	172.69
		202.19	199.29	196.59	193.49	190.69	187.49	183.99	180.19	176.19	173.09
	Sn−10 wt.%Pb	204.32	206.22	205.62	203.72	201.52	198.12	195.32	191.62	187.92	181.42
		206.42	207.42	206.02	203.52	200.72	197.62	194.22	190.82	186.92	182.02
		207.12	207.82	205.92	203.62	200.82	197.62	194.12	190.72	186.92	182.52
		206.72	207.62	206.02	203.62	201.02	197.62	194.42	190.42	187.22	183.12
		206.32	206.82	205.62	203.32	200.62	197.72	194.12	190.52	186.82	183.02
	Sn−6.5 wt.%Pb	203.40	205.69	205.79	204.98	203.17	200.78	197.71	194.13	188.28	181.46
		203.14	204.82	205.39	204.79	203.19	201.08	198.27	194.45	189.84	184.08
		202.00	203.87	204.88	204.55	203.13	201.05	198.38	195.16	190.79	182.93
		199.09	202.33	203.97	203.95	202.65	200.98	198.66	195.65	189.56	179.11
		197.30	201.36	203.50	203.43	202.49	200.96	198.70	195.11	188.58	176.91

Appendix C. Velocity field calculation

The present appendix provides the details concerning the discretization of the heat equation in the liquid zone (without latent heat).

The controlling heat equation:

$$\frac{\partial T}{\partial t} + \vec{U} \cdot \vec{\nabla} T = \alpha \nabla^2 T,$$

where α is the thermal diffusivity of the liquid alloy.

The heat equation is discretized by mean of finite difference method centered in space and first order off-centered in time.

$$\left[\frac{\partial T}{\partial t}\right]_{(i,j)} = \left(\frac{T(i,j,k) - T(i,j,k-\delta t)}{\delta t}\right)$$

$$\left[\vec{\nabla} T\right]_{(i,j)}^{k-\delta t/2} = \left[\left(\frac{T(i,j+1,k-\delta t/2) - T(i,j-1,k-\delta t/2)}{2\delta x}\right), \left(\frac{T(i+1,j,k-\delta t/2) - T(i-1,j,k-\delta t/2)}{2\delta y}\right)\right]$$

$$\left[\nabla^2 T\right]_{(i,j)}^{k-\delta t/2} = \left(\frac{T(i,j+1,k-\delta t/2)+T(i,j-1,k-\delta t/2)-2T(i,j,k-\delta t/2)}{\delta x^2}\right) + \left(\frac{T(i+1,j,k-\delta t/2)+T(i-1,j,k-\delta t/2)-2T(i,j,k-\delta t/2)}{\delta y^2}\right)$$

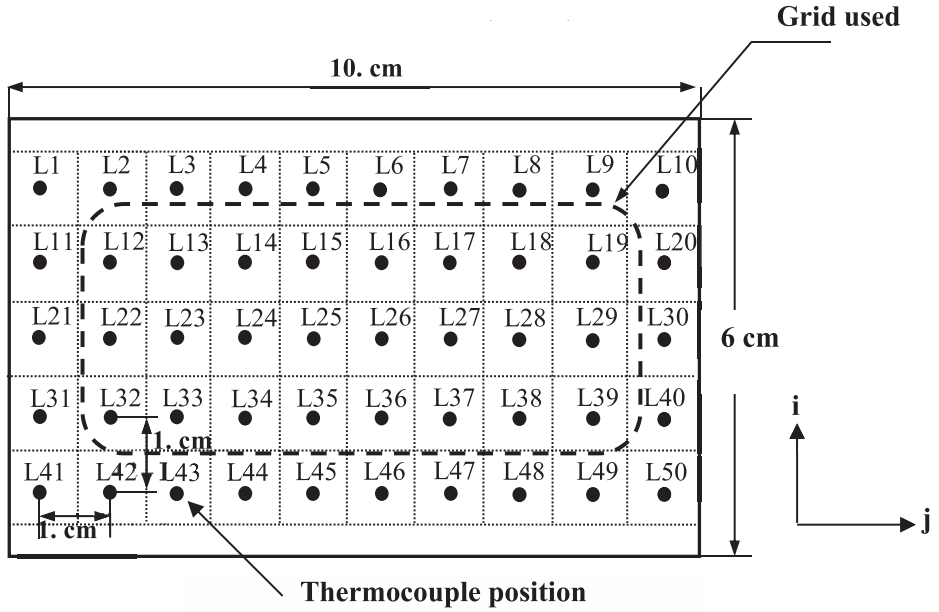

Fig. C.1. Grid of the points chosen for the calculation of the field dynamic represented in the zone limited par discontinuous line.

Appendix D. Geometric characteristics of the macrostructure of Sn–3 wt.% Pb, Sn–6.5 wt.% and Sn–10 wt.% Pb. Experimental conditions ΔT = 40 K, CR = 0.03 K/s.

Grain size mm^2	Area μm^2			Area percentage (%)			Number of grains		
	3%	6.5%	10%	3%	6.5%	10%	3%	6.5%	10%
x < 2	170.4	235.9	319.0	1.94	2.94	4.21	298	431	558
2 > x > 5	246.2	282.2	384.9	2.81	3.52	5.08	77	91	121
5 > x > 10	244.4	362.6	469.4	2.79	4.53	6.20	36	51	64
10 > x > 20	401.7	462.4	573.3	4.58	5.77	7.57	30	32	40
20 > x > 40	415.0	336.3	508.0	4.74	4.20	6.71	14	12	19
40 > x > 80	665.4	451.3	522.1	7.59	5.63	6.90	13	8	10
80 > x > 160	206.3	237.0	991.7	2.35	2.96	1.31	2	2	1
160 > x > 320	691.0	710.4	437.5	7.89	8.87	5.78	3	3	2
320 > x > 640	125.9	803.7	620.5	14.37	10.04	8.20	3	2	1
x > 640	0	642.9	0	0	8.03	0	0	1	0

Appendix E. Measurements of secondary dendritic spacing (λ_2) of Sn–3 wt.% Pb, Sn–6.5 wt.% and Sn–10 wt.% Pb. Experimental conditions ΔT = 40 K, CR = 0.03 K/s.

SDAS (μm)								
Sn–3 wt.%Pb			Sn–6.5 wt.%Pb			Sn–10 wt.%Pb		
Left part	Middle	Right part	Left part	Middle	Right part	Left part	Middle	Right part
99	90	91	94	92	86	75	68	64

References

[1] S.L. Braga, R. Viskanta, Int. J. Heat Mass Transfer 33 (1990) 745–754.
[2] D. Poulikakos, Numer. Heat. Transfer 14 (1988) 113–126.
[3] M.S. Christenson, F.P. Incropera, Int. J. Heat Mass Transfer 32 (1989) p.47–68.
[4] W. Kurz, D.J. Fisher, fourth revised ed., Trans Tech Publication Ltd., 1998.
[5] L.S. Chao, Y.R. Chen, H.Ch. Peng, W.S. Li, J. Chin. Inst. Eng. 31 (5) (2008) 729–735.
[6] Y.Y. Jin, Q.J. Wang, Z.Q. Chen, in: Joint Conference of Third International Symposium on Heat Transfer, Beijing and Fifth International Symposium on Transport Phenomena, Beijing, China, 1992.
[7] G. Quillet, A. Ciobanas, P. Lehmann, Y. Fautrelle, Int. J. Heat Mass Transfer 50 (2007) 654–666.

[8] L. Hachani, B. Saadi, X.D. Wang, A. Nouri, K. Zaidat, A. Belgacem-Bouzida, L. Ayouni-Derouiche, G. Raimondi, Y. Fautrelle, Int. J. Heat Mass Transfer 55 (2012) 1986–1996.
[9] X.D. Wang, P. Petitpas, C. Garnier, J.P. Paulin, Y. Fautrelle, Int. J. Heat Mass Transfer 335 (2007) 336–341.
[10] L. Hachani, J. Wang, I. Kaldre, G. Salloum Abou-Jaoude, O. Budenkova, G. Reinhart, K. Zaidat, N. Mangelinck, X. Li, H. Nguyen Thi, A. Bojarevics, Z.-M. Ren, L. Buligins, Y. Fautrelle, Mater. Sci. Forum 790–791 (2014) 375–383.
[11] J.N. Koster, R. Derebail, Heat Mass Transfer 32 (1997) 489–498.
[12] R. Boussaa, O. Budenkova, L. Hachani, X.D. Wang, B. Saadi, K. Zaidat, H. Ben Hadid, Y. Fautrelle, CFD Modeling and Simulation in Materials Processing, 2012, pp. p163–170.
[13] T. Carozzani, C.A. Gandin, H. Digonnet, M. Bellet, K. Zaidat, Y. Fautrelle, Met. Mater. Trans. A 44 (2) (2012) 873–887.
[14] S. Liu, S.Z. Lu, A. Hellawell, J. Cryst. Growth 234 (2002) 740.
[15] J.P. Gu, C. Beckermann, A.F. Giamei, Metall. Mater. Trans. A 28 (1997) 1533.
[16] M.A. Martorano, C. Beckermann, Ch.-A. Gandin, Metall. Mater. Trans. A 25 (2003) 1657.
[17] A. Badillo, C. Beckermann, Acta Mater. 54 (2006) 2015–2026.
[18] C.A. Siqueira, N. Cheung, A. Garcia, J. Alloys Compd. 351 (2003) p.126–134.
[19] S.V. Stankus, R.A. Khairulin, High Temp. 44 (3) (2006) 389–395.
[20] H. Thresh, A. Crawley, Metall. Mater. Trans. B 1 (6) (1970) 1531–1535.
[21] V.P. Osipenko, Russ. Phys. J. 13 (12) (1970) 1570–1573.
[22] R.A. Khairulin, S.V. Stankus, P.P. Bezverkhy, J. Alloys Compd. 312 (2000) 211–218.